

Refractory Plasmonic Hafnium Nitride and Zirconium Nitride Thin Films as Alternatives to Silver for Solar Mirror Applications

Prasanna Das, Bidesh Biswas, Krishna Chand Maurya, Magnus Garbrecht, and Bivas Saha*

Cite This: <https://doi.org/10.1021/acsami.2c09852>

Read Online

ACCESS |



Metrics & More



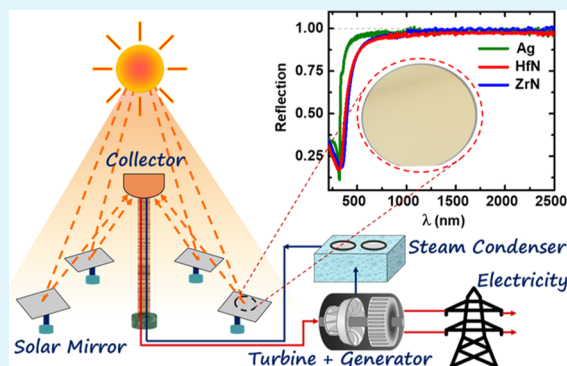
Article Recommendations



Supporting Information

ABSTRACT: Harnessing solar energy by employing concentrated solar power (CSP) systems requires materials with high electrical conductivity and optical reflectivity. Silver, with its excellent optical reflectance, is traditionally used as a reflective layer in solar mirrors for CSP technologies. However, silver is soft and expensive, quickly tarnishes, and requires a protective layer of glass for practical applications. Moreover, supply-side constraints and high-temperature instability of silver have led to the search for alternative materials that exhibit high solar and infrared reflectance. Transition metal nitrides, such as titanium nitride, have emerged as alternative plasmonic materials to gold starting from a spectral range of ~ 500 nm. However, to achieve high solar reflection (~ 320 – 2500 nm), materials with epsilon-near-zero starting from the near-ultraviolet (UV) spectral region are required. Here, we show the development of refractory epitaxial hafnium nitride (HfN) and zirconium nitride (ZrN) thin films as excellent mirrors with a solar reflectivity of $\sim 90.3\%$ and an infrared reflectivity of $\sim 95\%$. Low-loss and high-quality epsilon-near-zero resonance at near-UV (~ 340 – 380 nm) spectral regions are achieved in HfN and ZrN by carefully controlling the stoichiometry, leading to a sharp increase in the reflection edge that is on par with silver. Temperature-dependent reflectivity and dielectric constants are further measured to demonstrate their high-temperature suitability. The development of refractory epitaxial HfN and ZrN thin films with high solar and infrared reflectance makes them excellent alternative plasmonic materials to silver and would pave their applications in CSP, daytime radiative cooling, and others.

KEYWORDS: concentrated solar power, solar mirror, transition metal nitrides, alternative plasmonic materials, ultrahigh vacuum deposition, refractory nanophotonics



INTRODUCTION

Solar technologies are an essential component of sustainable renewable energy that is harnessed by converting light into other forms of energy. Photovoltaics (PV) aims to convert sunlight directly into electricity, whereas concentrated solar power (CSP) uses heat or thermal energy from sunlight as an intermediate to generate electricity.¹ Solar technologies have a substantial positive impact on the energy demand of the modern world by providing low-cost, pollution-free, low-carbon-emission energy.² One of the main components of CSP technology is a solar mirror or reflector, which is used to focus a large area of sunlight onto a small area of the collector.³ The concentrated light is then used as heat to generate electricity via a turbine. An ideal solar reflector should have very high solar reflectance, specularly, low maintenance cost, and a long lifetime.⁴

Silver (Ag) is widely used in solar mirrors due to its very high optical reflectance of $\sim 96\%$, which is the highest for any metal, and its low surface roughness and smoothness at the atomic level.^{5,6} However, silver's softness, low melting temperature (~ 960 °C), and corrosive nature prevent its

application in harsh conditions and at high temperatures. Additionally, an extra layer of transparent glass made of SiO_2 or TiO_2 is always used to protect silver films.⁷ Due to such constraints and the limited reserves of silver, efforts are underway to search for alternative materials to replace silver. As a potential candidate, aluminum (Al) exhibits reflectivity in the range of 85–90% in the visible to near-ultraviolet (UV) spectral region.⁸ However, Al shows a reflectance drop between 800 and 900 nm, which limits its utility. Similarly, gold (Au), nickel (Ni), chromium (Cr), platinum (Pt), and copper (Cu) can be utilized in the solar mirror due to their moderately high solar reflectance, but they also suffer from various atmospheric conditions. Dielectric mirrors based on one or more transparent dielectric materials can reflect up to

Received: June 2, 2022

Accepted: September 23, 2022

99.99% of light at a single wavelength.⁹ Still, their efficiency is limited to a narrow bandwidth of the solar spectrum. Therefore, it is crucial to develop solar mirrors with very high specular reflectance materials that are also hard, less expensive, corrosion-resistant, and stable at high temperatures.

Transition metal nitrides (TMNs), such as titanium nitride (TiN), have recently emerged as alternative plasmonic materials to noble metals in the visible to near-infrared (IR) spectral region.^{10–14} Apart from the excellent tunable optical properties, TiN possesses high hardness, excellent thermal stability, and complementary metal–oxide–semiconductor (CMOS) compatibility. In addition, the high corrosion resistance of TiN makes it a suitable plasmonic material in extremely harsh conditions. Therefore, TiN has been a material of choice for many practical applications such as durable optical coatings,¹⁵ solar absorbers,¹⁶ solar cell contacts,¹⁷ and refractive index sensors.¹⁸ Recently, it was reported that MBE-deposited TiN exhibits a very high reflectance of more than 90% at near-infrared spectral ranges, similar to gold.¹⁹ However, TiN reflects solar irradiation starting from ~500 nm to longer wavelengths due to its epsilon-near-zero (ENZ) wavelength (positive-to-negative crossover of the real part of dielectric permittivity) of ~500 nm. As a result, the reflection of the entire solar spectrum is not possible with TiN, which precludes its applicability in solar mirrors.

Similar to TiN, TMNs like hafnium nitride (HfN) and zirconium nitride (ZrN) are also refractory, mechanically hard (hardness of ~22–24 GPa), and thermally stable and possess high electrical conductivity and high optical reflectivity.^{20–22} Both HfN and ZrN exhibit large melting temperatures of ~3305 and 2980 °C, respectively, which are higher than that of TiN. As a result, HfN and ZrN are also emerging as promising candidates for applications in hot carrier solar cells,²³ metamaterial absorbers,²⁴ solar-driven water evaporation,²⁵ and thermal imprinting of plasmonic hotspots.²⁶ HfN and ZrN films exhibit ENZ at ~340–380 nm, similar to Ag. Utilizing HfN and ZrN as metallic components, HfN/ScN and ZrN/ScN metal/semiconductor superlattices are also developed that exhibit both type-I and type-II hyperbolic photonic dispersion starting from the near-UV to near-IR spectral ranges.²⁷ However, despite their ENZ at ~340 to ~380 nm, which is close to the edge of the solar spectrum at short wavelengths, the measured reflectivity values of HfN and ZrN are relatively small (68 and 75% in the 320–900 nm range, respectively).^{28,29} Such a lower reflection coefficient results from a somewhat tapered rise in the reflection edge from its plasma frequency or ENZ point due to higher optical losses. As a result, neither of these two materials has been considered for solar mirror applications. Since a high solar reflection coefficient of more than ~90% is necessary for solar mirrors, efforts must be made to increase their reflectivity.

Fortunately, unlike noble metals, the optical properties of TMNs can be tuned by changing the growth conditions. Previous work has shown that high substrate temperature gives rise to better crystal quality with the high reflectance of HfN films.²⁸ Under low deposition pressure, highly crystalline films are formed as incident particles encounter fewer collision events.³⁰ HfN_x films are also prepared by varying the stoichiometry with changing nitrogen concentration.³¹ In near-stoichiometric films, a significant increase in the electron mean free path leads to higher reflectivity. Negative substrate bias also improves optical reflectivity due to reduced nitrogen and hafnium vacancies in the film.^{32,33} Similarly, the optical

properties of ZrN are also improved by tuning the growth parameters.^{34–36} However, simultaneous tuning of all of the growth parameters to achieve the highest optical reflectivity achievable in HfN and ZrN films remains unexplored. In this work, we demonstrate record-high solar and infrared reflectance of epitaxial stoichiometric HfN and ZrN thin films by optimizing all of the growth parameters. Temperature-dependent reflectivity and dielectric constants of the films are measured, firmly establishing the utility of HfN and ZrN as a replacement for Ag for solar mirror applications.

EXPERIMENTAL DETAILS

Stoichiometric and epitaxial HfN and ZrN thin films are deposited on (001) MgO substrates with ultrahigh vacuum reactive direct current (DC) magnetron sputtering with a base pressure of 1×10^{-9} Torr at a substrate temperature of 900 °C. The thicknesses of HfN and ZrN thin films are ~400 and ~200 nm, respectively, which are more than their optical decay lengths (~45–50 nm). Details about the growth method are presented in the Supporting Information Section. Optimized conditions for achieving epitaxial and stoichiometric HfN and ZrN thin films are presented in Table 1.

Table 1. Deposition Parameters Used to Grow Epitaxial HfN and ZrN Thin Films

target power (W)	deposition pressure (mTorr)	deposition temperature (°C)	Ar/N ₂ (sccm)	substrate bias (W)
75	3	900	15:1	15

To compare the optical properties, a 150 nm thick Ag film is further deposited with electron beam evaporation at a base pressure of 10^{-6} Torr. Structural and microscopic properties of the films are measured with high-resolution X-ray diffraction (HRXRD), field-emission scanning electron microscopy (FESEM), atomic force microscopy (AFM), and high-resolution (scanning) transmission electron microscopy (HR(S)/TEM) techniques. X-ray photoelectron spectroscopy (XPS) of optimized HfN films is performed to check chemical composition and to find the stoichiometric ratio. Reflectivity and dielectric constants (wavelength range from 210 to 2500 nm) are measured using J.A. Woollam RC2 spectroscopic ellipsometer attached to a cryostat operating at a temperature range from 100 to 700 K. The infrared reflection is measured with Bruker Fourier transform infrared spectroscopy (FTIR) measurements. Details about the characterization methods are presented in the Supporting Information Section.

RESULTS AND DISCUSSION

Structural Characterization. HRXRD measurement (see Figure 1a) shows that sputter-deposited HfN (Figure 1b) and ZrN thin films (Figure S1a) grow with (002) orientations on (001) MgO substrates. Corresponding to the 002 diffraction peak located at 39.45 and 39.15°, HfN and ZrN exhibit out-of-plane (*c*-axis) lattice constants of 4.54 and 4.59 Å, respectively, that are consistent with previous literature reports.^{20,37} The full width at half-maximum (FWHM) of the rocking curve (ω -scan) for HfN (inset of Figure 1a) exhibits a value of 1.9°, which indicates its mosaic spread and epitaxial growth. As the substrate (MgO) exhibits the same rock salt crystal structure, HfN grows with the [001] (001) HfN || [001] (001) MgO epitaxial relationship. Four equally spaced (90° apart) asymmetric φ -peaks (see Figure S1b) confirm epitaxial growth of the HfN and ZrN films on MgO substrates. The AFM micrograph of a HfN film exhibits a smooth surface with a root-mean-square (RMS) roughness of 0.55 nm (Figure 1c), whereas ZrN film shows an RMS roughness of 0.7 nm (see

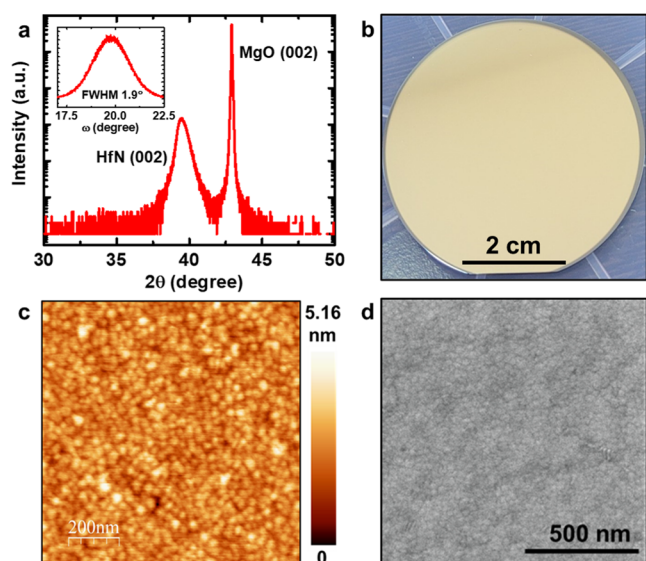


Figure 1. (a) High-resolution X-ray diffraction pattern of the HfN thin film deposited on the (001) MgO substrate showing 002 oriented growth. The rocking curve is shown in the inset. (b) Optical image of a HfN thin film (thickness \sim 400 nm) showing laguna yellow color. (c) Atomic force micrograph (AFM) of the HfN film exhibits an RMS roughness of 0.55 nm, and (d) scanning electron microscopy (SEM) image of the HfN film shows the formation of square-shaped mound structures.

Figure S1c in the Supporting Information). The slightly smaller RMS surface roughness of HfN could be related to its slightly higher melting temperature of \sim 3305 $^{\circ}$ C compared to the melting temperature of 2980 $^{\circ}$ C in ZrN as well as a lesser amount of lattice mismatch with the substrate MgO. The surface smoothness of the HfN film is also confirmed with plan-view FESEM images (see Figure 1d), which corroborates the AFM results. Small square-shaped, densely packed features observed on HfN films arise due to the formation of mound structures that exhibit 4-folds symmetry for rock salt crystals. These mound structures were also observed previously in sputter-deposited TiN and ScN.^{38,39} For the ZrN film, these square-shaped features are absent, and a more smooth surface can be seen in the FESEM image of the film presented in Figure S1d. X-ray photoelectron spectroscopy (XPS) measurements of the HfN film show Hf 4f and N 1s peaks (see Figure S4) with their binding energies that correspond to the Hf–N bond formation. From the area of the photoelectron spectrum, a Hf-to-N atomic ratio of 1.05 is calculated, which confirms the stoichiometric nature of the film.

A representative low-magnification STEM image of the HfN/MgO film (see Figure 2a) demonstrates the formation of a sharp interface between the HfN film and the MgO substrate. The atomic-resolution STEM image of the HfN/MgO interface (Figure 2b) highlights the cubic epitaxial growth of HfN on the MgO substrate with an orientation relationship of [001] (001) HfN \parallel [001] (001) MgO. As Hf atoms are heavier than Mg atoms, the HfN layer appears brighter than the MgO substrate in the STEM image. Misfit dislocations are observed at the HfN/MgO interface due to a \sim 6% lattice mismatch between the HfN and MgO layers. Elemental energy-dispersive X-ray spectroscopy (EDS) maps of Hf and N presented in Figure 2c,d, respectively, demonstrate uniform distributions of atoms in the HfN thin film. EDS spectra also show the

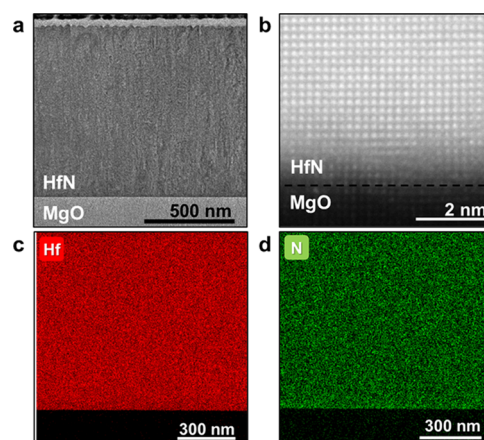


Figure 2. (a) Low-magnification STEM micrograph of a HfN film deposited on the (001) MgO substrate shows a uniform HfN layer and a sharp interface with the MgO substrate. (b) High-resolution STEM image of the HfN/MgO interface exhibits epitaxial cubic crystal growth. STEM-EDS elemental maps of (c) Hf and (d) N show uniform distribution within the film.

presence of oxygen in the films, a common unwanted impurity in transition metal nitrides.

Optical Characterization. Variable-angle spectroscopic ellipsometry (VASE) is used to determine the ambient temperature dielectric permittivity of HfN, ZrN, and Ag by fitting the experimental (ψ , Δ) spectra with a combination of the Drude–Lorentz model at three different angles of incidence (55 , 65 , and 75°). Results show that the real component of dielectric permittivity (ϵ') exhibits positive-to-negative crossover at 325, 350, and 380 nm for Ag, HfN, and ZrN, respectively (see Figure 3a), which represents the onset

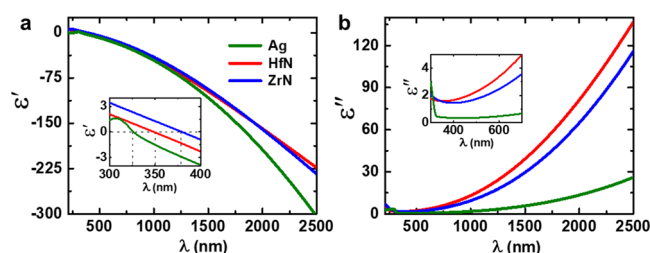


Figure 3. (a) Real and (b) imaginary components of dielectric permittivity (measured with spectroscopic ellipsometry from 210 to 2500 nm) of Ag, HfN, and ZrN films. The inset in (a) zooms into the wavelength range of 300–400 nm showing ϵ' positive-to-negative crossover of the films. The inset in (b) indicates the low optical loss of these films in the visible spectral range (400–700 nm).

of their metallic (plasmonic) characteristics. As the wavelength increases, ϵ' becomes more negative and displays a minimum of -305 , -224 , and -234 at 2500 nm for Ag, HfN, and ZrN, respectively. Ag exhibits the highest negative value of ϵ' due to its higher free-electron concentration and carrier relaxation times. The optical loss represented by the imaginary part of dielectric permittivity (ϵ'') is lowest for Ag, followed by ZrN and HfN (see Figure 3b). In the visible spectral range, ϵ'' of the three films remains small. However, ϵ'' increases monotonically with the wavelength in the near-infrared region due to free carrier absorption. Although the optical loss in HfN and ZrN is greater than Ag in the near-infrared region due to lower free-electron relaxation times (τ , see Figure 5a), the

relatively low loss in the near-UV wavelength (inset of Figure 3b) would make HfN and ZrN attractive for various exotic near-zero-index (NZI) properties, such as light tunneling,⁴⁰ time refraction,⁴¹ and diverging velocity.⁴²

To behave as a solar mirror, materials must specularly reflect the entire solar spectrum (320–2500 nm). Therefore, angle-dependent specular reflection of HfN and ZrN films is measured along with Ag with a spectroscopic ellipsometer (see Figure 4a,b). Results show that HfN and ZrN exhibit

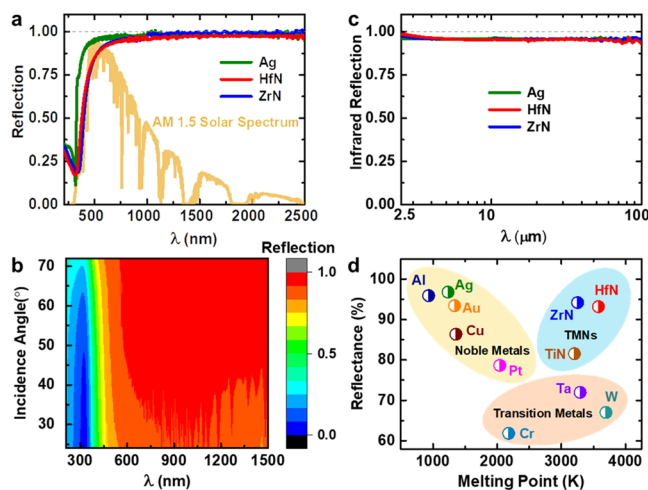


Figure 4. (a) Specular reflection of Ag, HfN, and ZrN films (measured with spectroscopic ellipsometry) with the AM 1.5 solar spectrum. (b) Angle-dependent reflection of the HfN film shows that the film exhibits very high reflection over all angles of incidence. (c) A Fourier transform infrared spectrometer measured the IR reflection of Ag, HfN, and ZrN films. (d) Comparison of integrated reflectance (320–2500 nm) and melting point among noble metals, transition metals, and TMNs.^{19,43,44}

integrated specular reflectance values (ratio of the area under the specular reflection curve and the ideal reflection curve at one particular angle of incidence) of 93.2 and 94.2%, respectively, at an angle of incidence of 64°, resembling the same of 96.8% for Ag (see Figure 4a). Away from the ENZ wavelength, i.e., from ~800 to 2500 nm, all three films are highly reflective (with reflectivity close to unity, see Figure 4c also). The reflection decreases near the ENZ region and exhibits a minimum at 317, 342, and 320 nm for HfN, ZrN, and Ag, respectively, consistent with their plasmonic nature. The sharpness of the reflection edge is determined by the Drude relaxation time (τ) of free electrons in metals.⁴⁵ As τ is smaller for HfN and ZrN compared to that for Ag ($\tau_{\text{HfN}} \sim 3.2$ fs, $\tau_{\text{ZrN}} \sim 4$ fs, and $\tau_{\text{Ag}} \sim 23.5$ fs), their reflection edge is less sharp than Ag. As the optimized stoichiometric and epitaxial HfN and ZrN films exhibit lesser defect and impurity densities, their τ values are much larger than those containing a higher concentration of defects (see the Supporting Information). A comparison of the reflectivity spectra of HfN and ZrN in this work and previously reported studies (see Figure S7 in Supporting Information) also highlights the improvements in this work. Nevertheless, further improvement of film quality is expected to result in a sharper rise in the reflectivity edge and, therefore, would increase the solar reflectivity. The effect of surface morphology on the optical properties of HfN is studied and confirms that the film grown with optimized conditions exhibits lesser surface defects and RMS roughness (see

Supporting Information). Angle-dependent reflectivity shows high reflection over the entire angles of incidence for both HfN (see Figure 4b) and ZrN (see Figure S10d), which further highlights the usefulness of these materials as solar mirrors. It is important to note that HfN and ZrN films deposited on Si and quartz substrates also with optimized deposition conditions exhibit very high reflectivity (see the Supporting Information), making them attractive for practical applications.

The solar reflectance of the films is further evaluated using

the relation $R_S = \frac{\int_{320\text{nm}}^{2500\text{nm}} R(\lambda)I(\lambda)d\lambda}{\int_{320\text{nm}}^{2500\text{nm}} I(\lambda)d\lambda}$, where $R(\lambda)$ and $I(\lambda)$ are the

reflection spectrum and solar spectrum, respectively.⁸ The calculated solar reflectance values at an angle of incidence of 64° are 90.2 and 90.3% for HfN and ZrN films, respectively, indicating that these films are proficiently reflecting the entire solar spectrum. Further, the solar reflectance is measured by integrating sphere-based UV–visible spectroscopy over the entire hemisphere, showing that HfN and ZrN films exhibit reflectance values of ~88 and 89%, respectively, compared to 95% in Ag (see Supporting Information). Though the solar reflectivity values of the HfN and ZrN films are lower than that of Ag (96%), they are still higher than those of most metallic films under investigation for solar mirrors and are comparable to that of Al. While Al is considered a replacement for Ag, along with the softness, low melting temperature, and stability issues, Al also shows a decrease in reflectivity between 800 and 900 nm, a significant bottleneck for its applications. A comparative plot of specular reflectance and melting point (see Figure 4d) highlights the superiority of HfN and ZrN over noble and transition metals used in solar mirrors.⁴⁴ Therefore, given the excellent material properties, HfN and ZrN thin films could serve as an alternative to Ag not only for applications where Ag cannot work due to material constraints but also for applications where the high reflectivity criterion is relaxed to an extent. High solar reflection in HfN and ZrN thin films will be useful not only for CSP technologies but also for selective absorbers in solar thermal applications. Since the nitride films reflect more than 90% of the incident solar radiation, several solar thermal techniques such as water heaters, solar fuels, and furnace technologies would benefit from these materials.

Along with the high reflectivity in the solar spectrum, solar mirrors must also exhibit high reflectivity in the infrared spectral range. Fourier transform infrared spectroscopy is used to measure reflection in the infrared region from 2.5 to 100 μm . Figure 4c shows that HfN and ZrN thin films provide 94.8 and 95.4% infrared reflectance, similar to Ag (95.5%), which would make these films suitable for durable infrared reflective coatings on night vision systems,⁴⁶ large infrared telescopes,⁴⁷ and pointing and tracking systems.⁴⁶

Next, we computed various surface plasmon polariton (SPP) parameters for HfN, ZrN, and Ag from experimental dielectric permittivity and compared them with those for Au and TiN (see Figure 5). The propagation length (L) and decay length (δ) serve as performance metrics for waveguiding applications for propagating plasmons at the metal–air interface.^{49,50} SPPs propagating at the interface follow the following dispersion relation

$$k_{\text{SPP}} = \frac{2\pi}{\lambda} \sqrt{\frac{\epsilon_m \epsilon_a}{\epsilon_m + \epsilon_a}} \quad (1)$$

where k_{SPP} , ϵ_m , and ϵ_a denote the propagation constant in the direction of propagation and the dielectric permittivities of

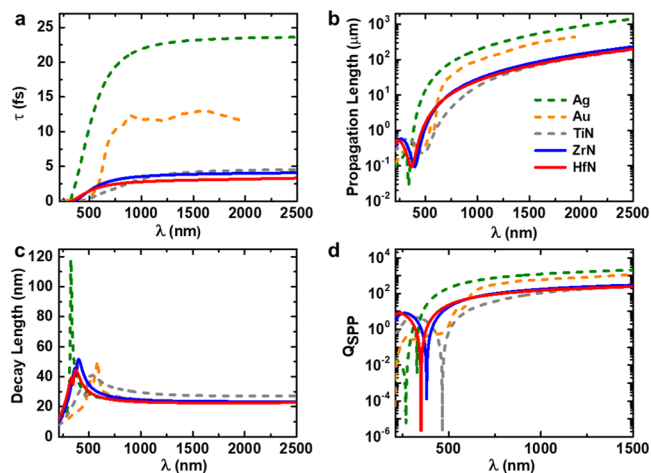


Figure 5. Comparison of (a) relaxation time (τ), (b) propagation length, (c) decay length, and (d) quality factor (Q_{SPP}) of HfN and ZrN films with Ag, Au, and TiN films. Optical constants of Au and TiN are adopted from Johnson and Christy et al. and Maurya et al., respectively.^{42,48}

metal and air, respectively.⁴⁹ The distance at which the energy of the surface plasmon decays by a factor of $1/e$ in the direction of propagation is defined as the propagation length, which is denoted by⁵⁰

$$L = \frac{1}{2\text{Im}(k_{\text{SPP}})} \quad (2)$$

SPP propagation starts when HfN and ZrN become plasmonic, i.e., after the ENZ wavelength, and the propagation length increases as the wavelength increases, exhibiting large values of 200 and 233 μm at 2500 nm, respectively (see Figure 5b). The electromagnetic field of the surface plasmon shows the maximum value at the metal–air interface and decays perpendicularly into the two media. The decay length is defined as the distance from the interface at which the field falls off by $1/e$, which is given as follows⁵⁰

$$\delta = \frac{\lambda}{2\pi} \sqrt{\frac{|\epsilon'| + \epsilon_a}{|\epsilon_m|^2}} \quad (3)$$

Therefore, at the crossover wavelength when the real part becomes zero, the large decay length corresponds to very low loss. Silver having the lowest optical loss at the crossover wavelength ($\epsilon'' \sim 0.5$) exhibits a very high value of decay length. HfN and ZrN thin films possess optical losses of 2 and 1.5, respectively, at the respective crossover wavelengths, which are similar to those for plasmonic Au (~ 1.2) and TiN (~ 2.5). As expected, plasmon decay length exhibits a maximum of 45 and 52 nm at the ENZ wavelength for HfN and ZrN, respectively, which indicates their very good plasmonic response (Figure 5c). The quality factor for surface plasmon polariton defined by $Q_{\text{SPP}} = \frac{\epsilon'^2}{\epsilon''}$ ⁵¹ serves as a performance figure of merit of the metal for plasmonic applications. Results show that HfN and ZrN exhibit higher values of the quality factor ($Q_{\text{HfN}} \sim 242$ and $Q_{\text{ZrN}} \sim 298$ at $\lambda = 1500$ nm) from visible to near-infrared spectral ranges (Figure 5d).

Temperature-dependent dielectric constants are measured from 100 to 700 K at an angle of incidence of 70° using a cryostat attached to the spectroscopic ellipsometer. During the temperature-dependent measurement, the cryostat chamber is

kept under a high vacuum of 10^{-7} Torr to eliminate any possibilities of surface oxidation. Real (Figure 6a) and

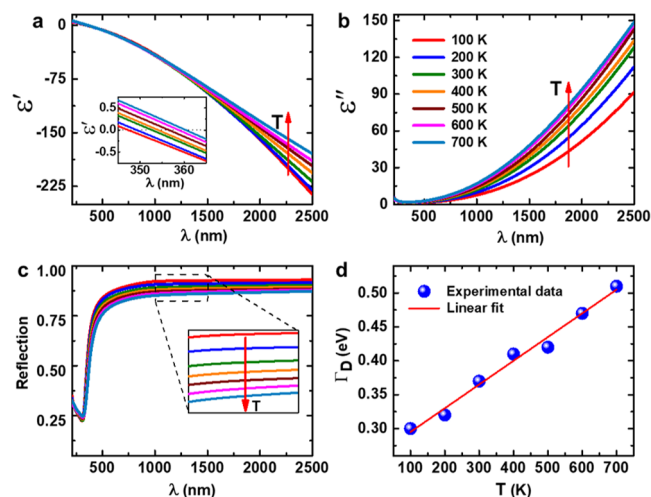


Figure 6. Temperature-dependent optical properties: (a) real (ϵ') and (b) imaginary (ϵ'') parts of the dielectric permittivity of the HfN film measured from the 100–700 K temperature range. (c) Reflection deduced from ϵ' and ϵ'' values at each temperature. (d) Linear variation of the Drude damping factor (Γ_D) with temperature.

imaginary (Figure 6b) components of the dielectric permittivity of HfN films are plotted along with the specular reflection (Figure 6c) derived from the permittivity at different temperatures. The dielectric permittivity depends on the plasma frequency (ω_p) and damping factor (Γ_D) by the following Drude relation

$$\epsilon(\omega) = \epsilon'(\omega) + i\epsilon''(\omega) = \frac{-\omega_p^2}{\omega^2 + i\Gamma_D\omega} \quad (4)$$

where $\epsilon' = \frac{-\omega_p^2}{\omega^2 + \Gamma_D^2}$ and $\epsilon'' = \frac{\omega_p^2\Gamma_D}{\omega^3 + \Gamma_D^2\omega}$.⁵²

The Drude damping factor Γ_D is related to different scattering phenomena arising from electron–phonon and electron–electron scattering. At very low temperatures, the electron–phonon scattering rate is low, which results in a smaller value of Γ_D (Figure 6d).^{52,53} However, as the temperature increases, electron–phonon scattering starts to increase rapidly, which in turn makes Γ_D larger. On the other hand, the plasma frequency (ω_p) depends on the effective mass (m^*) and free-electron concentration (n) as $\omega_p^2 = \frac{ne^2}{m^* \times \epsilon_0}$. With increasing temperature, n usually decreases due to the volume expansion described by the volume expansion coefficient γ as $n = \frac{n_0}{\sqrt{1 + \gamma(T - T_0)}}$, where n_0 is the electron concentration at temperature T_0 .⁵⁴ As a result, ω_p decreases with temperature, and the ENZ wavelength of HfN continuously shifts toward the long-wavelength regime with an increasing temperature (see the inset of Figure 6a). The simultaneous reduction in plasma frequency and increase in damping constant result in a decrease of the magnitude of ϵ' with temperature (see Figure 6a). At the same time, the imaginary part of dielectric permittivity (ϵ'') increases with temperature (Figure 6b) due to the increased scattering. Such behavior of the changes in the optical constants with increasing temperatures was also found in other transition metal nitrides such as TiN and noble metals

such as Ag.^{52–54} Temperature-dependent reflection has been retrieved from the measured dielectric constants at each temperature (see Figure 6c), suggesting that the high reflection properties of HfN films prevail at high temperatures, which is consistent with previous work on HfN-based nanodisk arrays.⁵⁵ However, a slight decrease in reflection occurs in the near-infrared range due to a change in permittivity with temperature (inset of Figure 6c). HfN exhibits a solar reflectance loss of ~7% when its temperature increases from 100 to 700 K, whereas Ag shows a decrease of ~5% in reflection as its temperature elevated to 840 from 90 K.⁵⁶ Therefore, the overall temperature dependence of the reflection of HfN is well comparable to that of Ag. Temperature-dependent optical properties of ZrN films are presented in the Supporting Information, showing similar trends as HfN. Therefore, not only at ambient, HfN and ZrN can serve as a replacement for Ag in high-temperature applications as well. In addition, the excellent thermal stability of HfN and ZrN enhances the possibility of their use in solar probes, which require a sun shield that can withstand temperatures of about 1370 °C and reduces sunlight absorption by reflecting most of the solar irradiation.

CONCLUSIONS

In summary, we show that sputter-deposited epitaxial and stoichiometric HfN and ZrN films can replace silver for solar mirror applications. HfN and ZrN thin films exhibit high solar reflection of ~90.3% and infrared reflection of ~95%, which are higher than those of most of the alternative metals studied for solar mirrors thus far. Structural characterization reveals that HfN and ZrN grow as an epitaxial film with cube-on-cube epitaxy on (001) MgO substrates and possess very low surface roughness. Temperature-dependent optical properties show that these films can preserve their high reflectivity at high temperatures. Record-high reflectivity, large mechanical hardness, structural and thermal stability, high melting temperatures, and CMOS compatibility make HfN and ZrN attractive alternative materials for solar mirrors in photovoltaics,⁵⁷ heat-assisted magnetic recordings,⁵⁸ high-brightness light-emitting diode (LED) devices,⁵⁹ and passive daytime radiative cooling applications.⁶⁰

ASSOCIATED CONTENT

Data Availability Statement

Data are available on request from the authors.

Supporting Information

The Supporting Information is available free of charge at <https://pubs.acs.org/doi/10.1021/acsami.2c09852>.

Growth conditions; characterization methods, structural and temperature-dependent optical properties of the ZrN film; effect of surface morphology on optical properties; comparison of reflection with previous works; comparison of the mechanical and optical properties of HfN and ZrN with those of the Ag film (PDF)

AUTHOR INFORMATION

Corresponding Author

Bivas Saha – Chemistry and Physics of Materials Unit, Jawaharlal Nehru Centre for Advanced Scientific Research, Bangalore 560064, India; International Centre for Materials Science and School of Advanced Materials, Jawaharlal Nehru

Centre for Advanced Scientific Research, Bangalore 560064, India; orcid.org/0000-0002-0837-1506; Email: bsaha@jncasr.ac.in, bivas.mat@gmail.com

Authors

Prasanna Das – Chemistry and Physics of Materials Unit, Jawaharlal Nehru Centre for Advanced Scientific Research, Bangalore 560064, India; International Centre for Materials Science, Jawaharlal Nehru Centre for Advanced Scientific Research, Bangalore 560064, India

Bidesh Biswas – Chemistry and Physics of Materials Unit, Jawaharlal Nehru Centre for Advanced Scientific Research, Bangalore 560064, India; International Centre for Materials Science, Jawaharlal Nehru Centre for Advanced Scientific Research, Bangalore 560064, India

Krishna Chand Maurya – Chemistry and Physics of Materials Unit, Jawaharlal Nehru Centre for Advanced Scientific Research, Bangalore 560064, India; International Centre for Materials Science, Jawaharlal Nehru Centre for Advanced Scientific Research, Bangalore 560064, India

Magnus Garbrecht – Sydney Microscopy and Microanalysis, The University of Sydney, Camperdown, New South Wales 2006, Australia

Complete contact information is available at:

<https://pubs.acs.org/doi/10.1021/acsami.2c09852>

Notes

The authors declare no competing financial interest.

ACKNOWLEDGMENTS

P.D. and B.S. acknowledge the International Centre for Materials Science (ICMS) and Sheikh Saqr Laboratory (SSL) of Jawaharlal Nehru Centre for Advanced Scientific Research (JNCASR) for support. B.S. acknowledges Ras Al Khaimah Centre for Advanced Materials and Raknor LLC for financial support. M.G. acknowledges the facilities of Sydney Microscopy and Microanalysis at The University of Sydney. P.D. and K.C.M. thank the Council of Scientific & Industrial Research (CSIR) for the fellowship. P.D. thanks Dheemahi Rao and Dr. Nidhi Pandey for FESEM measurements and XPS data analyses. P.D. and B.S. thank Dr. Pralay K. Santra and Modasser Hossain for UV–visible–near-IR spectroscopy measurements.

REFERENCES

- (1) Barlev, D.; Vidu, R.; Stroeve, P. Innovation in Concentrated Solar Power. *Sol. Energy Mater. Sol. Cells* **2011**, *95*, 2703–2725.
- (2) Tyagi, V. V.; Rahim, N. A. A.; Rahim, N. A.; Selvaraj, J. A. L. Progress in Solar PV Technology: Research and Achievement. *Renewable Sustainable Energy Rev.* **2013**, *20*, 443–461.
- (3) Guney, M. S. Solar Power and Application Methods. *Renewable Sustainable Energy Rev.* **2016**, *57*, 776–785.
- (4) Jamali, H. Investigation and Review of Mirrors Reflectance in Parabolic Trough Solar Collectors (PTSCs). *Energy Rep.* **2019**, *5*, 145–158.
- (5) Kennedy, C. E.; Terwilliger, K. Optical Durability of Candidate Solar Reflectors. *J. Sol. Energy Eng.* **2005**, *127*, 262–269.
- (6) Zheng, B.; Wong, L. P.; Wu, L. Y. L.; Chen, Z. Identifying Key Factors towards Highly Reflective Silver Coatings. *Adv. Mater. Sci. Eng.* **2017**, *2017*, 1–12.
- (7) Morales, A.; Durán, A. Sol-Gel Protection of Front Surface Silver and Aluminum Mirrors. *J. Sol-Gel Sci. Technol.* **1997**, *8*, 451–457.
- (8) Grosjean, A.; Soum-Glaude, A.; Thomas, L. Replacing Silver by Aluminum in Solar Mirrors by Improving Solar Reflectance with

- Dielectric Top Layers. *Sustainable Mater. Technol.* **2021**, *29*, No. e00307.
- (9) Braunstein, A. I.; Braunstein, M. High-Reflectivity Mirrors for Use at 10.6 Mm. *J. Vac. Sci. Technol.* **1971**, *8*, 412–418.
- (10) Naik, G. V.; Shalae, V. M.; Boltasseva, A. Alternative Plasmonic Materials: Beyond Gold and Silver. *Adv. Mater.* **2013**, *25*, 3264–3294.
- (11) Naik, G. V.; Schroeder, J. L.; Ni, X.; Kildishev, A. V.; Sands, T. D.; Boltasseva, A. Titanium Nitride as a Plasmonic Material for Visible and Near-Infrared Wavelengths. *Opt. Mater. Express* **2012**, *2*, 478–489.
- (12) Maurya, K. C.; Shalae, V. M.; Boltasseva, A.; Saha, B. Reduced Optical Losses in Refractory Plasmonic Titanium Nitride Thin Films Deposited with Molecular Beam Epitaxy. *Opt. Mater. Express* **2020**, *10*, 2679–2692.
- (13) Garbrecht, M.; Hultman, L.; Fawey, M. H.; Sands, T. D.; Saha, B. Tailoring of Surface Plasmon Resonances in TiN/(Al_{0.72}Sc_{0.28})N Multilayers by Dielectric Layer Thickness Variation. *J. Mater. Sci.* **2018**, *53*, 4001–4009.
- (14) Mascaretti, L.; Barman, T.; Bricchi, B. R.; Münz, F.; Li Bassi, A.; Kment, S.; Naldoni, A. Controlling the Plasmonic Properties of Titanium Nitride Thin Films by Radiofrequency Substrate Biasing in Magnetron Sputtering. *Appl. Surf. Sci.* **2021**, *554*, No. 149543.
- (15) Hu, C.; Guo, K.; Li, Y.; Gu, Z.; Quan, J.; Zhang, S.; Zheng, W. Optical Coatings of Durability Based on Transition Metal Nitrides. *Thin Solid Films* **2019**, *688*, No. 137339.
- (16) Liu, Z.; Liu, G.; Huang, Z.; Liu, X.; Fu, G. Ultra-Broadband Perfect Solar Absorber by an Ultra-Thin Refractory Titanium Nitride Meta-Surface. *Sol. Energy Mater. Sol. Cells* **2018**, *179*, 346–352.
- (17) Yang, X.; Liu, W.; De Bastiani, M.; Allen, T.; Kang, J.; Xu, H.; Aydin, E.; Xu, L.; Bi, Q.; Dang, H.; AlHabshi, E.; Kotsvos, K.; AlSaggaf, A.; Gereige, I.; Wan, Y.; Peng, J.; Samundsett, C.; Cuevas, A.; De Wolf, S. Dual-Function Electron-Conductive, Hole-Blocking Titanium Nitride Contacts for Efficient Silicon Solar Cells. *Joule* **2019**, *3*, 1314–1327.
- (18) Monfared, Y. E. Refractive Index Sensor Based on Surface Plasmon Resonance Excitation in a D-Shaped Photonic Crystal Fiber Coated by Titanium Nitride. *Plasmonics* **2020**, *15*, 535–542.
- (19) Guo, W.-P.; Mishra, R.; Cheng, C.-W.; Wu, B.-H.; Chen, L.-J.; Lin, M.-T.; Gwo, S. Titanium Nitride Epitaxial Films as a Plasmonic Material Platform: Alternative to Gold. *ACS Photonics* **2019**, *6*, 1848–1854.
- (20) Chakraborty, S.; Uchiyama, H.; Garbrecht, M.; Bhatia, V.; Pillai, A. I. K.; Feser, J. P.; Adroja, D. T.; Langridge, S.; Saha, B. Phononic Bandgap and Phonon Anomalies in HfN and HfN/ScN Metal/Semiconductor Superlattices Measured with Inelastic x-Ray Scattering. *Appl. Phys. Lett.* **2020**, *117*, No. 111901.
- (21) Garbrecht, M.; Schroeder, J. L.; Hultman, L.; Birch, J.; Saha, B.; Sands, T. D. Microstructural Evolution and Thermal Stability of HfN/ScN, ZrN/ScN, and Hf_{0.5}Zr_{0.5}N/ScN Metal/Semiconductor Superlattices. *J. Mater. Sci.* **2016**, *51*, 8250–8258.
- (22) Patsalas, P. Zirconium Nitride: A Viable Candidate for Photonics and Plasmonics? *Thin Solid Films* **2019**, *688*, No. 137438.
- (23) Thapa, B.; Dubajic, M.; Nielsen, M. P.; Patterson, R.; Conibeer, G.; Shrestha, S. In *Hot Carrier Dynamics in Nitrogen – Rich Hafnium Nitride Thin Film*, 47th IEEE Photovoltaic Specialists Conference (PVSC); IEEE, 2020; pp 0793–0797.
- (24) Baqir, M. A.; Choudhury, P. K.; Akhtar, M. N. ZrN Fractal-Graphene-Based Metamaterial Absorber in the Visible and near-IR Regimes. *Optik* **2021**, *237*, No. 166769.
- (25) Margeson, M. J.; Dasog, M. Plasmonic Metal Nitrides for Solar-Driven Water Evaporation. *Environ. Sci. Water Res. Technol.* **2020**, *6*, 3169–3177.
- (26) Askes, S. H. C.; Garnett, E. C. Ultrafast Thermal Imprinting of Plasmonic Hotspots. *Adv. Mater.* **2021**, *33*, No. 2105192.
- (27) Das, P.; Maurya, K. C.; Schroeder, J. L.; Garbrecht, M.; Saha, B. Near-UV-to-Near-IR Hyperbolic Photonic Dispersion in Epitaxial (Hf,Zr)N/ScN Metal/Dielectric Superlattices. *ACS Appl. Energy Mater.* **2022**, *5*, 3898–3904.
- (28) Farrell, I. L.; Reeves, R. J.; Preston, A. R. H.; Ludbrook, B. M.; Downes, J. E.; Ruck, B. J.; Durbin, S. M. Tunable Electrical and Optical Properties of Hafnium Nitride Thin Films. *Appl. Phys. Lett.* **2010**, *96*, No. 071914.
- (29) Mei, A. B.; Howe, B. M.; Zhang, C.; Sardela, M.; Eckstein, J. N.; Hultman, L.; Rockett, A.; Petrov, I.; Greene, J. E. Physical Properties of Epitaxial ZrN/MgO(001) Layers Grown by Reactive Magnetron Sputtering. *J. Vac. Sci. Technol., A* **2013**, *31*, No. 061516.
- (30) Liao, M. Y.; Gotoh, Y.; Tsuji, H.; Ishikawa, J. Growth and Stress Evolution of Hafnium Nitride Films Sputtered from a Compound Target. *J. Vac. Sci. Technol., A* **2004**, *22*, 214–220.
- (31) Hu, C.; Gu, Z.; Wang, J.; Zhang, K.; Zhang, X.; Li, M.; Zhang, S.; Fan, X.; Zheng, W. Nature of Tunable Optical Reflectivity of Rocksalt Hafnium Nitride Films. *J. Phys. Chem. C* **2014**, *118*, 20511–20520.
- (32) Gu, Z.; Wang, J.; Hu, C.; Zhang, X.; Dang, J.; Zhang, S.; Gao, J.; Wang, X.; Chen, H.; Zheng, W. Ion-Bombardment-Induced Reduction in Vacancies and Its Enhanced Effect on Conductivity and Reflectivity in Hafnium Nitride Films. *Appl. Phys. A* **2016**, *122*, No. 776.
- (33) Jeng, J.-S.; Liu, C.-H.; Chen, J. S. Effects of Substrate Bias and Nitrogen Flow Ratio on the Resistivity, Composition, Crystal Structure, and Reflectance of Reactively Sputtered Hafnium-Nitride Film. *J. Alloys Compd.* **2009**, *486*, 649–652.
- (34) Meng, J.; Fu, Z.; Du, M.; Liu, X.; Hao, L. Influence of Ion-Atom Arrival Ratio on Structure and Optical Properties of ZrN x Films. *Mater. Lett.* **2016**, *164*, 291–293.
- (35) Veszelei, M.; Andersson, K.; Ribbing, C.-G.; Järrendahl, K.; Arwin, H. Optical Constants and Drude Analysis of Sputtered Zirconium Nitride Films. *Appl. Opt.* **1994**, *33*, 1993–2001.
- (36) Benia, H. M.; Guemmaz, M.; Schmerber, G.; Mosser, A.; Parlebas, J. C. Optical Properties of Non-Stoichiometric Sputtered Zirconium Nitride Films. *Appl. Surf. Sci.* **2003**, *211*, 146–155.
- (37) Garbrecht, M.; McCarroll, I.; Yang, L.; Bhatia, V.; Biswas, B.; Rao, D.; Cairney, J. M.; Saha, B. Thermally Stable Epitaxial ZrN/Carrier-Compensated Sc_{0.99}Mg_{0.01}N Metal/Semiconductor Multilayers for Thermionic Energy Conversion. *J. Mater. Sci.* **2020**, *55*, 1592–1602.
- (38) Burmistrova, P. V.; Maassen, J.; Favaloro, T.; Saha, B.; Salamat, S.; Koh, Y. R.; Lundstrom, M. S.; Shakouri, A.; Sands, T. D. Thermoelectric Properties of Epitaxial ScN Films Deposited by Reactive Magnetron Sputtering onto MgO(001) Substrates. *J. Appl. Phys.* **2013**, *113*, No. 153704.
- (39) Achour, A.; Porto, R. L.; Soussou, M.-A.; Islam, M.; Boujita, M.; Aissa, K. A.; Le Brizoual, L.; Djouadi, A.; Brousse, T. Titanium Nitride Films for Micro-Supercapacitors: Effect of Surface Chemistry and Film Morphology on the Capacitance. *J. Power Sources* **2015**, *300*, 525–532.
- (40) Silveirinha, M.; Engheta, N. Tunneling of Electromagnetic Energy through Subwavelength Channels and Bends Using ϵ -Near-Zero Materials. *Phys. Rev. Lett.* **2006**, *97*, No. 157403.
- (41) Zhou, Y.; Alam, M. Z.; Karimi, M.; Upham, J.; Reshef, O.; Liu, C.; Willner, A. E.; Boyd, R. W. Broadband Frequency Translation through Time Refraction in an Epsilon-near-Zero Material. *Nat. Commun.* **2020**, *11*, No. 2180.
- (42) Khurgin, J. B.; Clerici, M.; Bruno, V.; Caspani, L.; DeVault, C.; Kim, J.; Shaltout, A.; Boltasseva, A.; Shalae, V. M.; Ferrera, M.; Faccio, D.; Kinsey, N. Adiabatic Frequency Shifting in Epsilon-near-Zero Materials: The Role of Group Velocity. *Optica* **2020**, *7*, 226–231.
- (43) Sárosi, Z.; Knapp, W.; Kunz, A.; Wegener, K. In *Evaluation of Reflectivity of Metal Parts by a Thermo-Camera*, InfraMation 2010 Proceedings, 2010; pp 475–486.
- (44) Maurya, K. C.; Biswas, B.; Rao, D.; Saha, B. Giant Enhancement of Plasmonic Response and Epsilon-near-Zero Signature in Refractory Transition Metals (Ta, W, and Mo) Deposited at High-Temperature. *Appl. Phys. Lett.* **2021**, *118*, No. 041902.

- (45) Delin, A.; Eriksson, O.; Ahuja, R.; Johansson, B.; Brooks, M. S. S.; Gasche, T.; Auluck, S.; Wills, J. M. Optical Properties of the Group-IV B Refractory Metal Compounds. *Phys. Rev. B* **1996**, *54*, 1673–1681.
- (46) Rogalski, A.; Chrzanowski, K. Infrared Devices And Techniques (Revision). *Metrol. Meas. Syst.* **2014**, *21*, 565–618.
- (47) Rayner, J. T.; Toomey, D. W.; Onaka, P. M.; Denault, A. J.; Stahlberger, W. E.; Vacca, W. D.; Cushing, M. C.; Wang, S. SpeX: A Medium-Resolution 0.8–5.5 Micron Spectrograph and Imager for the NASA Infrared Telescope Facility. *Publ. Astron. Soc. Pac.* **2003**, *115*, 362–382.
- (48) Johnson, P. B.; Christy, R. W. Optical Constants of the Noble Metals. *Phys. Rev. B* **1972**, *6*, 4370–4379.
- (49) Maier, S. A. *Plasmonics: Fundamentals and Applications*; Springer: New York, 2007; Vol. 76.
- (50) Homola, J. Electromagnetic Theory of Surface Plasmons. In *Springer Series on Chemical Sensors and Biosensors*; Springer, 2006; pp 3–44.
- (51) Blaber, M. G.; Arnold, M. D.; Ford, M. J. A Review of the Optical Properties of Alloys and Intermetallics for Plasmonics. *J. Phys.: Condens. Matter* **2010**, *22*, No. 143201.
- (52) Reddy, H.; Guler, U.; Kudyshev, Z.; Kildishev, A. V.; Shalaev, V. M.; Boltasseva, A. Temperature-Dependent Optical Properties of Plasmonic Titanium Nitride Thin Films. *ACS Photonics* **2017**, *4*, 1413–1420.
- (53) Briggs, J. A.; Naik, G. V.; Zhao, Y.; Petach, T. A.; Sahasrabudhe, K.; Goldhaber-Gordon, D.; Melosh, N. A.; Dionne, J. A. Temperature-Dependent Optical Properties of Titanium Nitride. *Appl. Phys. Lett.* **2017**, *110*, No. 101901.
- (54) Reddy, H.; Guler, U.; Chaudhuri, K.; Dutta, A.; Kildishev, A. V.; Shalaev, V. M.; Boltasseva, A. Temperature-Dependent Optical Properties of Single Crystalline and Polycrystalline Silver Thin Films. *ACS Photonics* **2017**, *4*, 1083–1091.
- (55) Chiao, Z.-Y.; Chen, Y.-C.; Chen, J.-W.; Chu, Y.-C.; Yang, J.-W.; Peng, T.-Y.; Syong, W.-R.; Lee, H. W. H.; Chu, S.-W.; Lu, Y.-J. Full-Color Generation Enabled by Refractory Plasmonic Crystals. *Nanophotonics* **2022**, *11*, 2891–2899.
- (56) Winsemius, P. Temperature Dependence of the Optical Properties Ag: The X-Point. *Phys. Status Solidi* **1973**, *59*, K55–K58.
- (57) Rahman, R.; Khan, M. F. In *Performance Enhancement of PV Solar System by Mirror Reflection*, International Conference on Electrical & Computer Engineering (ICECE 2010); IEEE, 2010; pp 163–166.
- (58) Gosciniak, J.; Justice, J.; Khan, U.; Corbett, B. Study of TiN Nanodisks with Regard to Application for Heat-Assisted Magnetic Recording. *MRS Adv.* **2016**, *1*, 317–326.
- (59) Yum, W.-S.; Jeon, J.-W.; Sung, J.-S.; Jin, S.; Seong, T.-Y. Ag/Ni/Ag Multilayer Reflector for GaN-Based Vertical Light-Emitting Diode. *Jpn. J. Appl. Phys.* **2013**, *52*, No. 052101.
- (60) Raman, A. P.; Anoma, M. A.; Zhu, L.; Rephaeli, E.; Fan, S. Passive Radiative Cooling below Ambient Air Temperature under Direct Sunlight. *Nature* **2014**, *515*, 540–544.